Biomedical Optics EXPRESS

Depth resolved detection of lipid using spectroscopic optical coherence tomography

Christine P. Fleming,[1,*] Jocelyn Eckert,[2] Elkan F. Halpern,[3] Joseph A. Gardecki,[2] and Guillermo J. Tearney[2,4]

[1]*Columbia University, Department of Electrical Engineering, New York, New York, USA*
[2]*Wellman Center for Photomedicine, Massachusetts General Hospital, Boston, Massachusetts, USA*
[3]*Radiology Division, Massachusetts General Hospital, Boston, Massachusetts, USA*
[4]*Department of Pathology, Massachusetts General Hospital, Boston, Massachusetts, USA*
**cfleming@ee.columbia.edu*

Abstract: Optical frequency domain imaging (OFDI) can identify key components related to plaque vulnerability but can suffer from artifacts that could prevent accurate identification of lipid rich regions. In this paper, we present a model of depth resolved spectral analysis of OFDI data for improved detection of lipid. A quadratic Discriminant analysis model was developed based on phantom compositions known chemical mixtures and applied to a tissue phantom of a lipid-rich plaque. We demonstrate that a combined spectral and attenuation model can be used to predict the presence of lipid in OFDI images.

OCIS codes: (110.4500) Optical coherence tomography; (170.1580) Chemometrics; (170.6510) Spectroscopy, tissue diagnostics.

References and links

1. V. L. Roger, A. S. Go, D. M. Lloyd-Jones, E. J. Benjamin, J. D. Berry, W. B. Borden, D. M. Bravata, S. Dai, E. S. Ford, C. S. Fox, H. J. Fullerton, C. Gillespie, S. M. Hailpern, J. A. Heit, V. J. Howard, B. M. Kissela, S. J. Kittner, D. T. Lackland, J. H. Lichtman, L. D. Lisabeth, D. M. Makuc, G. M. Marcus, A. Marelli, D. B. Matchar, C. S. Moy, D. Mozaffarian, M. E. Mussolino, G. Nichol, N. P. Paynter, E. Z. Soliman, P. D. Sorlie, N. Sotoodehnia, T. N. Turan, S. S. Virani, N. D. Wong, D. Woo, M. B. Turner, and M. Turner; American Heart Association Statistics Committee and Stroke Statistics Subcommittee, "Heart Disease and Stroke Statistics—2012 Update: A Report From the American Heart Association," Circulation **125**(1), e2–e220 (2012).
2. A. P. Burke, A. Farb, G. T. Malcom, Y.-H. Liang, J. Smialek, and R. Virmani, "Coronary Risk Factors and Plaque Morphology in Men with Coronary Disease who Died Suddenly," N. Engl. J. Med. **336**(18), 1276–1282 (1997).
3. A. V. Finn, M. Nakano, J. Narula, F. D. Kolodgie, and R. Virmani, "Concept of Vulnerable/Unstable Plaque," Arterioscler. Thromb. Vasc. Biol. **30**(7), 1282–1292 (2010).
4. G. J. Tearney, H. Yabushita, S. L. Houser, H. T. Aretz, I.-K. Jang, K. H. Schlendorf, C. R. Kauffman, M. Shishkov, E. F. Halpern, and B. E. Bouma, "Quantification of Macrophage Content in Atherosclerotic Plaques by Optical Coherence Tomography," Circulation **107**(1), 113–119 (2003).
5. A. Tanaka, G. J. Tearney, and B. E. Bouma, "Challenges on the frontier of intracoronary imaging: atherosclerotic plaque macrophage measurement by optical coherence tomography," J. Biomed. Opt. **15**(1), 011104 (2010).
6. Z. Wang, H. Kyono, H. G. Bezerra, H. Wang, M. Gargesha, C. Alraies, C. Xu, J. M. Schmitt, D. L. Wilson, M. A. Costa, and A. M. Rollins, "Semiautomatic segmentation and quantification of calcified plaques in intracoronary optical coherence tomography images," J. Biomed. Opt. **15**(6), 061711 (2010).
7. T. Kubo, T. Imanishi, S. Takarada, A. Kuroi, S. Ueno, T. Yamano, T. Tanimoto, Y. Matsuo, T. Masho, H. Kitabata, K. Tsuda, Y. Tomobuchi, and T. Akasaka, "Assessment of Culprit Lesion Morphology in Acute Myocardial Infarction: Ability of Optical Coherence Tomography Compared with Intravascular Ultrasound and Coronary Angioscopy," J. Am. Coll. Cardiol. **50**(10), 933–939 (2007).
8. D. Chamié, Z. Wang, H. Bezerra, A. M. Rollins, and M. A. Costa, "Optical Coherence Tomography and Fibrous Cap Characterization," Curr. Cardiovasc. Imaging Rep. **4**(4), 276–283 (2011).
9. H. Yabushita, B. E. Bouma, S. L. Houser, H. T. Aretz, I.-K. Jang, K. H. Schlendorf, C. R. Kauffman, M. Shishkov, D.-H. Kang, E. F. Halpern, and G. J. Tearney, "Characterization of Human Atherosclerosis by Optical Coherence Tomography," Circulation **106**(13), 1640–1645 (2002).
10. D. Levitz, L. Thrane, M. H. Frosz, P. Andersen, C. Andersen, S. Andersson-Engels, J. Valanciunaite, J. Swartling, and P. Hansen, "Determination of optical scattering properties of highly-scattering media in optical coherence tomography images," Opt. Express **12**(2), 249–259 (2004).

#189749 - $15.00 USD Received 2 May 2013; revised 14 Jun 2013; accepted 15 Jun 2013; published 5 Jul 2013

11. F. J. van der Meer, D. J. Faber, D. M. Baraznji Sassoon, M. C. Aalders, G. Pasterkamp, and T. G. van Leeuwen, "Localized Measurement of Optical Attenuation Coefficients of Atherosclerotic Plaque Constituents by Quantitative Optical Coherence Tomography," IEEE Trans. Med. Imaging **24**(10), 1369–1376 (2005).
12. F. J. van der Meer, D. J. Faber, J. Perrée, G. Pasterkamp, D. Baraznji Sassoon, and T. G. van Leeuwen, "Quantitative optical coherence tomography of arterial wall components," Lasers Med. Sci. **20**(1), 45–51 (2005).
13. C. Xu, J. M. Schmitt, S. G. Carlier, and R. Virmani, "Characterization of atherosclerosis plaques by measuring both backscattering and attenuation coefficients in optical coherence tomography," J. Biomed. Opt. **13**(3), 034003 (2008).
14. G. van Soest, T. Goderie, E. Regar, S. Koljenović, G. L. van Leenders, N. Gonzalo, S. van Noorden, T. Okamura, B. E. Bouma, G. J. Tearney, J. W. Oosterhuis, P. W. Serruys, and A. F. van der Steen, "Atherosclerotic tissue characterization in vivo by optical coherence tomography attenuation imaging," J. Biomed. Opt. **15**(1), 011105 (2010).
15. U. Morgner, W. Drexler, F. X. Kärtner, X. D. Li, C. Pitris, E. P. Ippen, and J. G. Fujimoto, "Spectroscopic optical coherence tomography," Opt. Lett. **25**(2), 111–113 (2000).
16. R. Leitgeb, M. Wojtkowski, A. Kowalczyk, C. K. Hitzenberger, M. Sticker, and A. F. Fercher, "Spectral measurement of absorption by spectroscopic frequency-domain optical coherence tomography," Opt. Lett. **25**(11), 820–822 (2000).
17. A. L. Oldenburg, C. Xu, and S. A. Boppart, "Spectroscopic Optical Coherence Tomography and Microscopy," IEEE J. Sel. Top. Quantum Electron. **13**(6), 1629–1640 (2007).
18. M. Kulkarn and J. A. Izatt, "Spectroscopic optical coherence tomography," in Conference on Lasers and Electro Optics, Vol. 9 of 1996 OSA Technical Digest Series (Optical Society of America, 1996), pp. 59–60.
19. D. J. Faber, E. G. Mik, M. C. G. Aalders, and T. G. van Leeuwen, "Light absorption of (oxy-)hemoglobin assessed by spectroscopic optical coherence tomography," Opt. Lett. **28**(16), 1436–1438 (2003).
20. D. J. Faber, E. G. Mik, M. C. G. Aalders, and T. G. van Leeuwen, "Toward assessment of blood oxygen saturation by spectroscopic optical coherence tomography," Opt. Lett. **30**(9), 1015–1017 (2005).
21. M. Laubscher, S. e. Bourquin, L. Froehly, B. Karamata, and T. Lasser, "Spectroscopic optical coherence tomography based on wavelength de-multiplexing and smart pixel array detection," Opt. Commun. **237**(4-6), 275–283 (2004).
22. H. Cang, T. Sun, Z.-Y. Li, J. Chen, B. J. Wiley, Y. Xia, and X. Li, "Gold nanocages as contrast agents for spectroscopic optical coherence tomography," Opt. Lett. **30**(22), 3048–3050 (2005).
23. R. N. Graf, F. E. Robles, X. Chen, and A. Wax, "Detecting precancerous lesions in the hamster cheek pouch using spectroscopic white-light optical coherence tomography to assess nuclear morphology via spectral oscillations," J. Biomed. Opt. **14**(6), 064030 (2009).
24. S. Takarada, T. Imanishi, Y. Liu, H. Ikejima, H. Tsujioka, A. Kuroi, K. Ishibashi, K. Komukai, T. Tanimoto, Y. Ino, H. Kitabata, T. Kubo, N. Nakamura, K. Hirata, A. Tanaka, M. Mizukoshi, and T. Akasaka, "Advantage of Next-Generation Frequency-Domain Optical Coherence Tomography Compared with Conventional Time-Domain System in the Assessment of Coronary Lesion," Catheter. Cardiovasc. Interv. **75**(2), 202–206 (2010).
25. W. Jaross, V. Neumeister, P. Lattke, and D. Schuh, "Determination of cholesterol in atherosclerotic plaques using near infrared diffuse reflection spectroscopy," Atherosclerosis **147**(2), 327–337 (1999).
26. T. W. de Bruin, C. B. Brouwer, M. van Linde-Sibenius Trip, H. Jansen, and D. W. Erkelens, "Different postprandial metabolism of olive oil and soybean oil: a possible mechanism of the high-density lipoprotein conserving effect of olive oil," Am. J. Clin. Nutr. **58**(4), 477–483 (1993).
27. U. G. Indahl, N. S. Sahni, B. Kirkhus, and T. Næs, "Multivariate strategies for classification based on NIR-spectra—with application to mayonnaise," Chemom. Intell. Lab. Syst. **49**(1), 19–31 (1999).
28. E. Stachowska, B. Dołęgowska, D. Chlubek, T. Wesołowska, K. Ciechanowski, P. Gutowski, H. Szumiłowicz, and R. A. Turowski, "Dietary trans fatty acids and composition of human atheromatous plaques," Eur. J. Nutr. **43**(5), 313–318 (2004).
29. P. Weinmann, M. Jouan, Q. D. Nguyen, B. Lacroix, C. Groiselle, J.-P. Bonte, and G. Luc, "Quantitative analysis of cholesterol and cholesteryl esters in human atherosclerotic plaques using near-infrared Raman spectroscopy," Atherosclerosis **140**(1), 81–88 (1998).
30. R. Manoharan, J. J. Baraga, M. S. Feld, and R. P. Rava, "Quantitative histochemical analysis of human artery using Raman spectroscopy," J. Photochem. Photobiol. B **16**(2), 211–233 (1992).
31. S. H. Yun, G. J. Tearney, B. J. Vakoc, M. Shishkov, W. Y. Oh, A. E. Desjardins, M. J. Suter, R. C. Chan, J. A. Evans, I.-K. Jang, N. S. Nishioka, J. F. de Boer, and B. E. Bouma, "Comprehensive volumetric optical microscopy in vivo," Nat. Med. **12**(12), 1429–1433 (2007).
32. J. M. Schmitt, A. Knüttel, M. Yadlowsky, and M. A. Eckhaus, "Optical-coherence tomography of a dense tissue: statistics of attenuation and backscattering," Phys. Med. Biol. **39**(10), 1705–1720 (1994).
33. R. J. Barnes, M. S. Dhanoa, and S. J. Lister, "Standard Normal Variae Transformation and De-trending of Near-Infrared Diffuse Reflectance Spectra," Appl. Spectrosc. **43**(5), 772–777 (1989).
34. L. Marcu, M. C. Fishbein, J.-M. I. Maarek, and W. S. Grundfest, "Discrimination of Human Coronary Artery Atherosclerotic Lipid-Rich Lesions by Time-Resolved Laser-Induced Fluorescence Spectroscopy," Arterioscler. Thromb. Vasc. Biol. **21**(7), 1244–1250 (2001).
35. S. K. Nadkarni, M. C. Pierce, B. H. Park, J. F. de Boer, P. Whittaker, B. E. Bouma, J. E. Bressner, E. Halpern, S. L. Houser, and G. J. Tearney, "Measurement of collagen and smooth muscle cell content in atherosclerotic

#189749 - $15.00 USD Received 2 May 2013; revised 14 Jun 2013; accepted 15 Jun 2013; published 5 Jul 2013

plaques using polarization-sensitive optical coherence tomography," J. Am. Coll. Cardiol. **49**(13), 1474–1481 (2007).
36. Z. Wang, H. Kyono, H. G. Bezerra, H. Wang, M. Gargesha, C. Alraies, C. Xu, J. M. Schmitt, D. L. Wilson, M. A. Costa, and A. M. Rollins, "Semiautomatic segmentation and quantification of calcified plaques in intracoronary optical coherence tomography images," J. Biomed. Opt. **15**(6), 061711 (2010).
37. S. K. Nadkarni, B. E. Bouma, J. de Boer, and G. J. Tearney, "Evaluation of collagen in atherosclerotic plaques: the use of two coherent laser-based imaging methods," Lasers Med. Sci. **24**(3), 439–445 (2009).
38. C.-L. Tsai, J.-C. Chen, and W.-J. Wang, "Near-infrared Absorption Property of Biological Soft Tissue Constituents," J. Med. Biol. Eng. **21**(1), 7–14 (2001).
39. C. Xu, D. L. Marks, M. N. Do, and S. A. Boppart, "Separation of absorption and scattering profiles in spectroscopic optical coherence tomography using a least-squares algorithm," Opt. Express **12**(20), 4790–4803 (2004).
40. B. Hermann, K. Bizheva, A. Unterhuber, B. Povazay, H. Sattmann, L. Schmetterer, A. Fercher, and W. Drexler, "Precision of extracting absorption profiles from weakly scattering media with spectroscopic time-domain optical coherence tomography," Opt. Express **12**(8), 1677–1688 (2004).
41. C. Xu, P. S. Carney, and S. A. Boppart, "Wavelength-dependent scattering in spectroscopic optical coherence tomography," Opt. Express **13**(14), 5450–5462 (2005).

1. Introduction

1.1 Coronary artery disease (CAD)

Coronary artery disease (CAD) is a progressive condition where lipid-containing plaques build up in the coronary artery wall, potentially leading to myocardial infarction or heart attack. In the United States, coronary artery disease is the cause of 1 in 6 deaths [1]. It has been shown that a large percentage of plaques that are prone to rupture and cause acute coronary syndromes have thin fibrous caps and large necrotic lipid pools, a high density of macrophages, and intraplaque hemmorage [2]. In a study to evaluate demographic and morphological variables to differentiate culprit versus non-culprit vulnerable plaques, of plaques with similar luminal narrowing, cap thickness and lipid-rich necrotic core were the only parameters that were significantly different between the culprit and non-culprit groups [3]. There is a great need to identify these high-risk plaques to predict which plaques that may go on to a myocardial infarction and prevent coronary events from occurring.

1.2 Optical coherence tomography characterization of plaques

Optical coherence tomography (OCT) and optical frequency domain imaging (OFDI), also known as Frequency Domain OCT (FD-OCT), provide subsurface imaging at depths up to 1-2 mm in biological tissue with high spatial resolution (10 μm axial resolution). Fiber-based OCT systems can be incorporated into catheters to image internal organs. These features have made OCT a powerful tool for cardiovascular imaging. Previous studies by our group and others have shown that OCT can identify key components related to plaque vulnerability such as lipid pools, macrophages [4,5], calcium [6], and cap thickness [7,8]. Currently lipid rich plaques are identified within OCT images as a signal poor region with diffuse boundaries [9]. The negative contrast for lipid places these OCT diagnoses at risk for misinterpretation due to artifacts and other causes of signal loss. A method for independently detecting the presence of lipid is therefore highly sought after.

Attenuation and backscattering analysis of axial scans using the single scattering model have been used to quantify the difference between fibro-calcific, fibrous, and lipid rich plaques [10–14]. From an *ex vivo*, histopathologic correlation study conducted by Xu et. al regions with lipid had a high attenuation coefficient and high backscattering coefficient. Whereas fibrous regions had a low attenuation coefficient and high backscattering coefficient, and calcific regions had a low attenuation coefficient and low backscattering coefficient [13]. van der Meer et. al conducted a correlative histopathology study of human carotid artery segments *ex vivo*, and measured the attenuation coefficient within the intima, media, lipid-rich regions, calcific regions and thrombus [5]. They were able to show significant differences in the attenuation coefficient within calcific and lipid-rich regions. However, in comparison to Xu et. al, they showed a significant decrease in attenuation coefficient within lipid-rich

#189749 - $15.00 USD Received 2 May 2013; revised 14 Jun 2013; accepted 15 Jun 2013; published 5 Jul 2013

regions. Van Soest has been recently translated attenuation analysis to catheter-based images of atherosclerotic plaques [14]. Stationary OCT images with ECG registration were obtained to analyze the effect of catheter and heart motion [14]. In this paper, we build upon this body of work by providing spectroscopic information that is complementary to the attenuation coefficient for plaque classification.

1.3 Objective

Our objective is to develop and validate an algorithm for automatic detection of lipid within OFDI images. Analysing the spectral signature of the acquired data can further enhance OCT discrimination of atherosclerotic plaques. We will employ spectroscopic OCT (SOCT), a post-processing technique that uses time-frequency analysis to generate depth resolved spectra [15–18]. SOCT has been used to analyze absorption due to oxy-and deoxy-hemoglobin [19,20], assess contrast enhancement using near infrared dyes [21] and nano-particles [22], and measure scattering dependent spectral modulations to detect precancerous lesions [23]. In this paper, we present the use of SOCT for automated classification of lipid through morphological and depth resolved spectroscopic analysis of optical frequency domain images. To explore the roles contributing to spectral differences, phantoms of increasing complexity were used.

2. Materials and methods

Near infrared basis spectra of pure substances related to plaque vulnerability and intravascular imaging (Fig. 1) were acquired with the Cary Varian spectrophotometer (Agilent Santa Clara, CA). The samples included cholesterol (Sigma, C8667), collagen (Sigma, C9879), calcium (Sigma Aldrich 289396), glycerol trioleate (Sigma, T7752), distilled water, omnipaque (GE Healthcare) and visipaque (GE Healthcare). For opaque samples, the Diffuse Reflectance Accessory with an integrating sphere was used. Within the bandwidth of the light source used for OFDI imaging in this study, λ_c = 1300nm, $\Delta\lambda$ = 100nm, water and cholesterol have nearly linear absorbance spectra. The water absorbance spectrum increases with wavelength whereas the cholesterol absorbance spectrum decreases with increasing wavelength (Figs. 1a, 1b). Calcium and collagen has a nearly flat absorbance spectrum over the wavelength region of the light source. Omnipaque and visipaque are common contrast agents used to flush the coronary artery during *in vivo* OCT imaging [24] and has similar absorbance spectra to water.

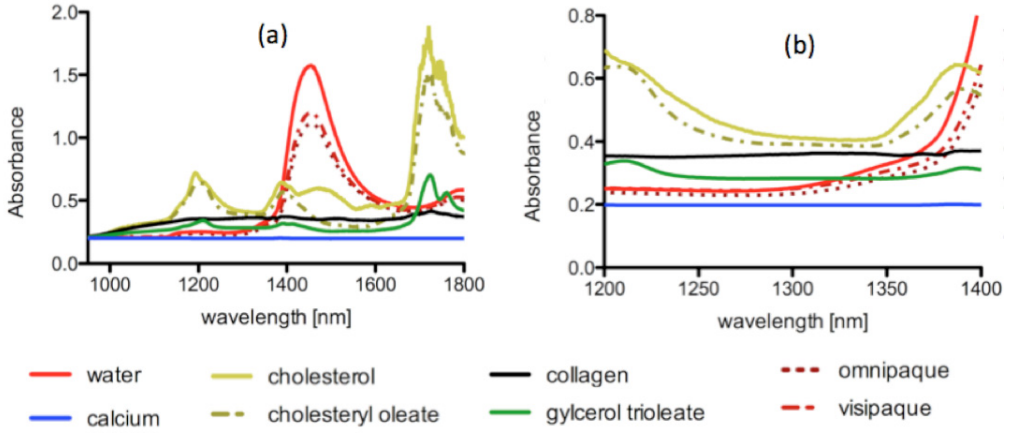

Fig. 1. (a) Near infrared absorbance spectra of pure substances related to plaque vulnerability and intravascular OCT imaging. (b) Absorbance spectra over OFDI source bandwidth. The wavelength range used within our study was 1250 to 1350 nm.

#189749 - $15.00 USD Received 2 May 2013; revised 14 Jun 2013; accepted 15 Jun 2013; published 5 Jul 2013

2.1 Cholesterol mixture phantoms

To evaluate the ability of SOCT to detect lipid, phantoms were created using solutions of known chemical compositions. A subset of the compounds shown in Fig. 1 were used to create the phantoms. Table 1 shows the compositions of first set of phantoms comprised of mixtures of cholesterol (Ch), collagen (Co), calcium (Ca), glycerol trioleate (T), and distilled water (W) to approximate the chemical composition of plaque. The phantom compositions were guided by a study by Jaross et al measuring chemical compositions within human atherosclerotic plaques [25]. To ensure that we were observing differences due to presence of cholesterol and not absence of water, compositions with 10, 20, and 30% calcium were also imaged. A mortar and pestle was used to prepare the compounds and make them as homogeneous as possible. Phantom compositions were placed in a quartz cuvette with a 1 mm path length for imaging.

Table 1. Composition of Phantoms

Phantom Name	Total Cholesterol [%]	Collagen [%]	Calcium [%]	Trioleate [%]	Water [%]	Sample size (images)
W	0	0	0	0	100	10
T	0	0	0	2	98	25
Ch10	10	0	0	2	88	24
Ch20	20	0	0	2	78	65
Ch30	30	0	0	2	88	45
Ca10	0	0	10	2	78	10
Ca20	0	0	20	2	68	10
Ca30	0	0	30	2	78	10
Co	0	8	0	2	68	20
CoCh10	10	8	0	2	68	35
CoCh20	20	8	0	2	90	60
CoCh30	30	8	0	2	80	40

2.2 Artificial lipid plaques

The second set of phantoms was designed to give the appearance of a lipid rich plaque within OFDI images. Artificial plaques were created by injecting fat emulsions (mayonnaise, Kraft) into the tunica media layer of fresh normal swine aorta. Mayonnaise was chosen as a fat emulsion for our phantom plaque because it is composed of soybean oil, which has primary lipid compositions of C18:2 (linoleic acid), C18:1 (oleic acid) and C16:0 (Palmitic acid) [26,27]. This has a similar lipid composition to coronary plaques, where the primary cholesterol oleate and cholesterol linoleate account for approximately 75 percent of all cholesterol esters [28–30]. In addition, mayonnaise was chosen over butter or oil because it is easily injectable and provides a scattering signature (data for butter and oil not shown). This will allow the evaluation of detecting a fat emulsion that is localized underneath a scattering media. Samples were imaged within 18 hours of sacrificing the animal. Tissue samples were placed in phosphate buffered saline. Imaging at room temperature (25° C) occurred directly after making the plaque phantoms.

2.3 Imaging protocol

All imaging was conducted with a custom built OFDI system, previously described [31]. Briefly, the system had a 1300 nm center wavelength, 100 nm bandwidth, and 52kHz axial line rate. 5 mm B-scan images were acquired of all samples. After imaging, a subset of the aortic phantom samples (n = 16) was placed in neutral buffered formalin for histological processing. Frozen cross sectional sections (10μm thickness) were stained Hemotoxylin and

#189749 - $15.00 USD Received 2 May 2013; revised 14 Jun 2013; accepted 15 Jun 2013; published 5 Jul 2013

Eosin (H&E). H&E sections were taken every 250μm throughout the volume were made for each sample. Slides were digitized using a NanoZoomer 2.0-HT slide scanner (Hamamatsu) at 20X.

2.4 Depth resolved spectral analysis

The short time Fourier transform (STFT) was used to generate depth resolved spectra. Windowed (Hanning) sections of the axial scan were Fourier transformed. There was a 90% overlap between successive windows, resulting in a 51μm axial resolution (in tissue) within the spectrogram. The spectrograms derived from 64 adjacent axial scans were averaged for final analysis. The single scattering model [Eq. (1)] was used to calculate the attenuation coefficient (from averaged axial lines) and the attenuation spectra (from averaged spectrograms). Within the first few hundred microns below the lumen surface, the axial intensity profile can be approximated by a first order model of scattering, where the backscatter intensity, I, decreases in an exponential manner as a function of axial depth, r [32]. The rate at which the intensity falls is attributed to the attenuation coefficient, μ_t, which is equal to the sum of the scattering and absorption coefficients. This model assumes that the region over which the attenuation coefficient is measured is homogeneous. For Fourier domain systems, an additional term is included to describe the signal fall off S(r), which is a function of the half width of the roll-off function, z_w, and position of the center of the scan after frequency shifting, z_c [14].

$$\begin{aligned} \left\langle I_d(r) \right\rangle &= I_o T(r) \hat{S}(r) \exp(-2\mu_t r) \\ T(r) &= \left[\left(\frac{r - z_o}{z_R} \right)^2 + 1 \right]^{-1/2} \\ \hat{S}(r) &= \exp\left[-\left(\frac{r - z_c}{z_w} \right)^2 \right]. \end{aligned} \tag{1}$$

Preprocessing was used to reduce the variability due to high frequency oscillations and intensity offsets in the attenuation spectra. A Savasky Golay filter, with a 4th order polynomial was used to smooth out the spectra and the standard normal variate (SNV) [Eq. (2)] reduce intensity differences while maintaining spectral shape [33].

$$SNV_i = \frac{I_i - \bar{I}}{\sqrt{\frac{\sum (I_i - \bar{I})^2}{n-1}}}. \tag{2}$$

2.5 Spectral parameter extraction and *classification model*

The preprocessed attenuation spectra, $\mu'_t(x, z, \lambda)$ can be described as a linear combination of the principal component spectra, $PC(\lambda)$, where the fitting coefficients, $c(x, z)$, are weights for each principal component spectra [Eq. (3)]. For the subsequent analysis, the first three principal component spectra ($PC_1(\lambda)$, $PC_2(\lambda)$, $PC_3(\lambda)$) were used for model fitting.

#189749 - $15.00 USD Received 2 May 2013; revised 14 Jun 2013; accepted 15 Jun 2013; published 5 Jul 2013

$$
\begin{aligned}
&PC(\lambda)c(x,z) = \mu_t(x,z,\lambda) \\
&\left[PC_1(\lambda)\ldots PC_n(\lambda)\right]\begin{bmatrix} c_1(x,z) \\ \vdots \\ c_n(x,z) \end{bmatrix} = \mu_t(x,z,\lambda) \\
&c = PC^{-1}\mu_t(x,z,\lambda) \\
&\mu_t(x,z,\lambda) \approx c_1(x,z)PC_1(\lambda) + c_2(x,z)PC_2(\lambda) + c_3(x,z)PC_3(\lambda).
\end{aligned}
\tag{3}
$$

The image set of phantoms outlined in Table 1 was used to develop a prediction model using quadratic discriminant analysis (Fig. 2). Inputs to the model included attenuation coefficient and spectral fitting coefficients. Model output was the probability for each pixel being assigned to the twelve compositions outlined in Table1 and the final classification (Fig. 3). The model was implemented in Matlab R2010b.

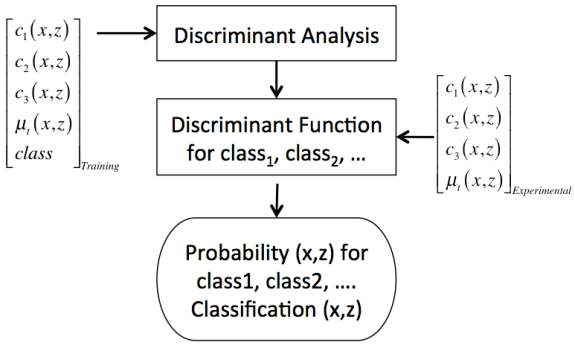

Fig. 2. Classification model using quadratic Discriminant analysis. The training data set consisted of fitting coefficients for the first three principal component spectra, pc1, pc2, pc3, the attenuation coefficient, and the class (composition outlined in Table 1). Quadratic Discriminant analysis was conducted discriminant functions to describe each class.

2.6 Statistical analysis

Results are presented as mean +/– standard deviation. Analysis of variance (ANOVA) with Tukey's multiple comparison tests was used for the evaluation of the significance of individual parameters. P-values less than 0.05 was considered statistically significant. McNemar's test was used to evaluate the outcome of classification models developed with (1) μ_t, (2) c_1, c_2, c_3, and (3) μ_t, c_1, c_2, c_3 by assessing which cases were misclassified by one model and not the other.

3. Results

3.1 Cholesterol phantom mixtures

The mean attenuation spectra of the twelve phantom compositions are shown in Fig. 3. Water (W) and 2% trioleate (T) had an increasing attenuation with increasing wavelength, whereas cholesterol had a decreasing attenuation with increasing wavelength. Calcium (Ca) phantoms had a relatively flat attenuation spectra. Phantoms with collagen (Co) and cholesterol (Ch) also exhibited a decrease in attenuation spectra with increasing wavelength. Preprocessing reduced high frequency spectral modulations and removed intensity bias (Figs. 4d-4f).

#189749 - $15.00 USD Received 2 May 2013; revised 14 Jun 2013; accepted 15 Jun 2013; published 5 Jul 2013

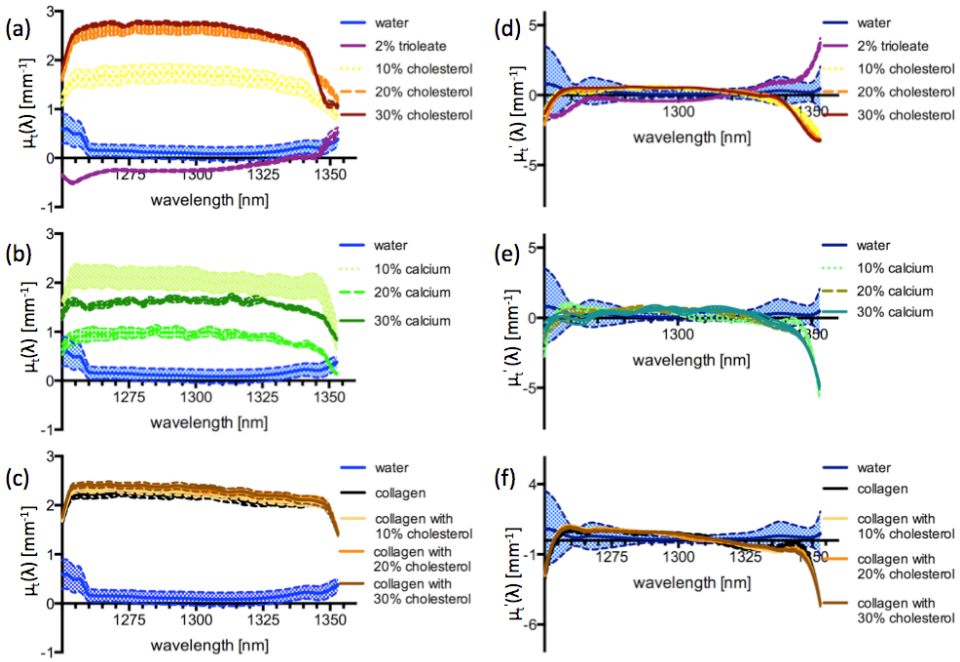

Fig. 3. Attenuation spectra measured using time frequency analysis from phantoms imaged within 1mm path length cuvette. (a) Attenuation spectra of phantoms composed of distilled water and varying concentrations of cholesterol. (b) Attenuation of phantoms composed of distilled water and various concentrations of calcium. (c) Attenuation of phantoms composed of distilled water, collagen, and various concentrations of cholesterol. (d-f) Preprocessing of attenuation spectra using SVN and a Savasky Golay filter corresponding to attenuation spectra in a-c. Preprocessing reduced intensity bias and high frequency oscillations to highlight spectral shape. The mean is plotted as a solid line with the shaded area representing the standard error.

The principal component spectra used in the model are shown in Fig. 4. The first three principal component spectra had eigenvalues of 580.6, 203.5, and 119.6 respectively, which together represented 76.90% of the energy within the data sets. The first principal component spectrum, PC1, resembles the absorbance spectra of water. Likewise, the second principal component spectrum resembles the cholesterol absorbance spectra. Figure 4 shows an example preprocessed attenuation spectra, obtained from a 624 µm region, is overlaid with the modeled spectra consisting of a linear combination of PC1, PC2, and PC3.

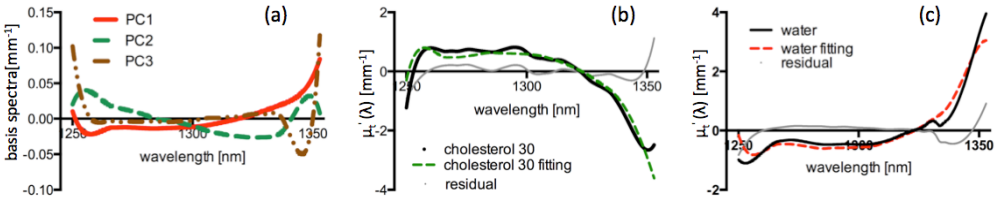

Fig. 4. Modeling attenuation spectra using principal component spectra. (a) Principal component spectra derived from principal component (PC) analysis. The first three PC spectra were included for modeling. (b) Example of preprocessed cholesterol 30% spectra (solid line). Fit is the linear combination of principal component spectra (dashed line). (c) Example of pure water preprocessed spectrum (solid line). Fit is the linear combination of principal component spectra (dashed line). Residuals of fit within (b) and (c) are shown in grey.

Figure 5 shows the normalized confusion matrices for the three models for classifying the phantoms outlined in Table 1. An ideal model will have ones (white) along the diagonal. As

#189749 - $15.00 USD Received 2 May 2013; revised 14 Jun 2013; accepted 15 Jun 2013; published 5 Jul 2013

can be seen in Fig. 5a, a large portion of collagen samples were misclassified as 30% cholesterol in the Discriminant model based on attenuation coefficient (μ_t) only. Likewise, the Discriminant model based on spectral fitting coefficients alone (Fig. 5b) had low discriminating power between samples with calcium and collagen. However, the combined algorithm (Fig. 5c), incorporating both attenuation and spectral fitting showed increased accuracy compared to models based on attenuation or spectral shape alone. Importantly, the magnitude of attenuation has poor correlation coefficients R^2 = 0.58, 0.02, 0.05 with spectral fitting coefficients c_1, c_2, and c_3 respectively, indicating that this the inclusion of spectroscopic data adds useful information.

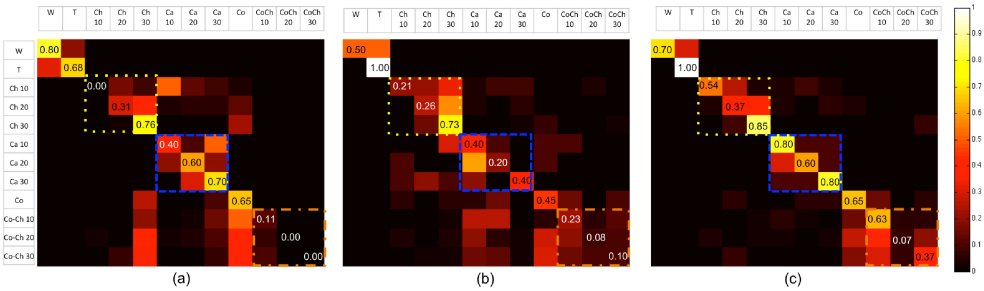

Fig. 5. Normalized confusion matrices are used to show the results of the Discriminant analysis model. (a) Model incorporating attenuation coefficients only. (b) Model incorporating spectral fitting coefficients only. (c) Model incorporating both attenuation coefficient and spectral fitting parameters. The classification accuracy improves significantly by combining information from both the magnitude of the attenuation coefficient and the spectral shape. Dashed lines indicate compositions with similar components but varying concentrations. Within the model incorporating spectral shape and magnitude of attenuation, we observe a high degree of misclassification between groups of similar components. W-water, T-trioleate, Ch-Cholesterol, Ca-Calcium, Co-Collagen, Co-Ch-Collagen and Cholesterol.

McNemar's test was conducted to evaluate if the addition of spectral information improved classification accuracy (Table 2) for the models presented in Fig. 5. Pair-wise comparisons of classification accuracy between quadratic discriminant analysis models with input parameters of attenuation, spectral fitting coefficients, and the combination of attenuation and spectral fitting coefficients were compared. The reference chi-squared value that for a p-value less than 0.05 and 11 degrees of freedom, $\chi^2_{(11,0.95)}$, was 19.675. Table 2 includes the χ^2 values for the pairwise comparisons, where bolded values indicate that models have a significantly different accuracy ($p<0.05$). Within our models for discriminating 12 different compositions, as outlined in Table 1, a model based on attenuation was not significantly different from a model based on spectral fitting coefficients. However, a model combining both attenuation and spectral fitting had a significantly improved accuracy than either parameter alone.

Table 2. McNemar's Values to Compare Discriminant Analysis Models Using Attenuation Coefficient and Spectral Fitting Parameters, Where the Output for the Model Are the 12 Compositions Described in Table 1*

Method variables (prediction rate)	Attenuation (31.69%)	Spectral Fitting (34.30%)	Attenuation and Spectral Fitting (50.29%)
Attenuation	NA	0.48	**47.61**
Spectral Fitting		NA	**37.21**
Attenuation and Spectral Fitting			NA

*Bolded values indicate that models have a statistically different accuracy.

From the confusion matrices in Fig. 5 we observe that all models did not have a large discrimination power for detecting concentrations. Within the combined model, phantoms

#189749 - $15.00 USD Received 2 May 2013; revised 14 Jun 2013; accepted 15 Jun 2013; published 5 Jul 2013

with a low concentration of cholesterol were misclassified as having a larger percentage of cholesterol. Likewise, phantoms with a low percentage of calcium were misclassified as having a large percentage of calcium. When we collapsed the groups Ch10, Ch20, and Ch30 into Ch, Ca10, Ca20, and Ca30 into Ca, and CoCh10, CoCh20, and CoCh30 into CoCh, we found that the overall predication rate for the combined model to 72.6%. The results of the quadratic Discriminant analysis models with the new classes are shown as confusion matrices in Fig. 6.

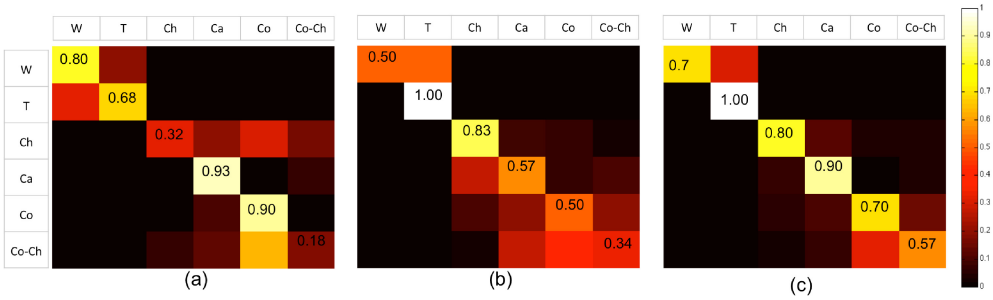

Fig. 6. Normalized Confusion matrices are used to show the results of the Discriminant analysis model. (a) Model incorporating attenuation coefficient. (b) Model incorporating spectral fitting coefficients. (c) A model incorporating both attenuation coefficient and spectral fitting parameters. The classification accuracy improves significantly by combining information from both the magnitude of the attenuation coefficient and the spectral shape. W-water, T-trioleate, Ch-Cholesterol, Ca-Calcium, Co-Collagen, Co-Ch-Collagen and Cholesterol.

McNemar's values for the models with 6 output classes (W-water, T-trioleate, Ch-Cholesterol, Ca-Calcium, Co-Collagen, Co-Ch-Collagen and Cholesterol) are shown in Table 3. The chi-squared value for a model with five degrees of freedom for a p-value less than 0.05, $\chi^2_{(5,0.95)}$, was 11.070. Table 3 includes pairwise comparisons of the model outputs, where bolded values indicate a significantly different accuracy. Within the model outputs for 6 classes, the discriminant model based on spectral fitting was more significant that the model of attenuation. Furthermore, the combined model of attenuation and spectral fitting had a significantly improved accuracy compared to models of attenuation or spectral fitting.

Table 3. McNemar's Values to Compare Discriminant Analysis Models of 6 Classes (W, T, Ch, Ca, Co, Co-Ch) Using Attenuation Coefficient and Spectral Fitting Parameters*

Method variables (prediction rate)	Attenuation (38.98%)	Spectral Fitting (60.45%)	Attenuation and Spectral Fitting (72.60%)
Attenuation	NA	**34.72**	**91.01**
Spectral Fitting		NA	**23.52**
Attenuation and Spectral Fitting			NA

*Bolded values indicate that models have a significantly different accuracy.

3.2 Lipid plaque phantoms

Since the cuvette based phantom models do not accurately model the attenuation characteristics of arterial tissue, the classification model using spectral fitting coefficients (Fig. 6b) was used for classification of tissue phantom plaques. Figure 7 is of a representative area of normal swine aorta. Cross sectional images within the volume (7b,7f) are shown with corresponding probability of cholesterol (7c,7g). A hue, saturation, value visualization method was used to display the full output of the model, encoding classification in hue and probability associated with the classification in saturation and value. Within our results, cholesterol is shown in yellow and collagen shown in red. As seen in panels 7d and 7h, the normal aorta had no pixels classified as cholesterol. This is further shown in the depth integrated probability

#189749 - $15.00 USD Received 2 May 2013; revised 14 Jun 2013; accepted 15 Jun 2013; published 5 Jul 2013

maps of cholesterol, 7i, and collagen, 7j. Within the data set of normal aorta, there was a low and probability of pixels classified as cholesterol and a high probability of pixels classified as collagen.

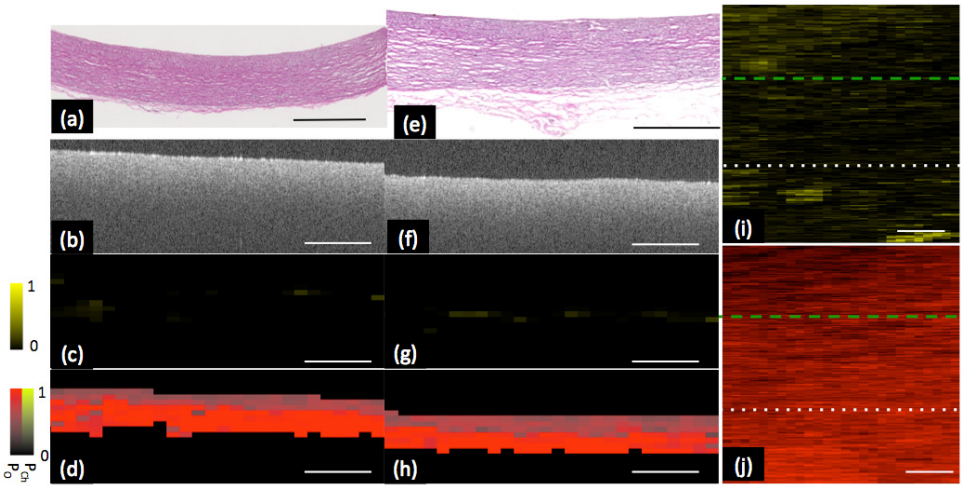

Fig. 7. Representative classification of normal swine aorta. Two sites within volumetric data set are shown in (a-d) and (e-h). H&E (a,e) of normal sites are shown for corresponding OFDI images (b,f). (c,g) Corresponding depth resolved probability maps for cholesterol are shown for OFDI images, with a model output of nearly no probability of cholesterol within images. (b,f). High probability of cholesterol appears yellow and low probability of cholesterol appears black. (d, h) Model output images incorporating classification and probability associate with the classification, where hue is dedicated as the class and probability associated with that classification encoded as value and saturation. Cholesterol – Yellow, Other – Red. (i) depth integration of cholesterol probability within volumetric OFDI data set showing low probability over volume of normal aorta. Low probability of lipid was coded as black and high probability of lipid was coded as bright yellow. (j) Depth integration of cholesterol probability within volumetric OFDI data set showing high probability over volume. Low probability of collagen was coded as black and high probability of collagen was coded as bright red. Scale bar 1mm.

To further evaluate the classification model, we developed phantoms to mimic the qualitative appearance of lipid rich plaques. An example of the lipid plaque is shown in panel 8b. Regions with the fat emulsion show a signal poor region with diffuse boundaries, consistent with the published qualitative description of lipid plaques [9]. This model allowed for a controlled evaluation of the classification model in the presence of both scattering and absorption.

Figure 8 depicts images from a representative lipid plaque phantom. Panels 8a-8d are of a region at the center of the plaque. Although the cap thickness is 0.79mm at the center, cholesterol is still detected within the depth resolved probability map of lipid (Fig. 8c) and classification image (Fig. 8d). Whereas, when the cap was 1.17mm thick at the edge of the injected emulsion (Figs. 8e-8h), cholesterol was not observable within the depth resolved probability image (Fig. 8g) or the classification image (Fig. 8h). This is important, as both OFDI images look similar (Figs. 8b,8f). Chemograms are shown in panels (i) and (j), depth-wise integrating the probability maps for cholesterol and collagen within the volume. The location of the injected fat emulsion is shown as a circular area with increased cholesterol probability (Fig. 8i) and decreased collagen probability (Fig. 8j).

#189749 - $15.00 USD Received 2 May 2013; revised 14 Jun 2013; accepted 15 Jun 2013; published 5 Jul 2013

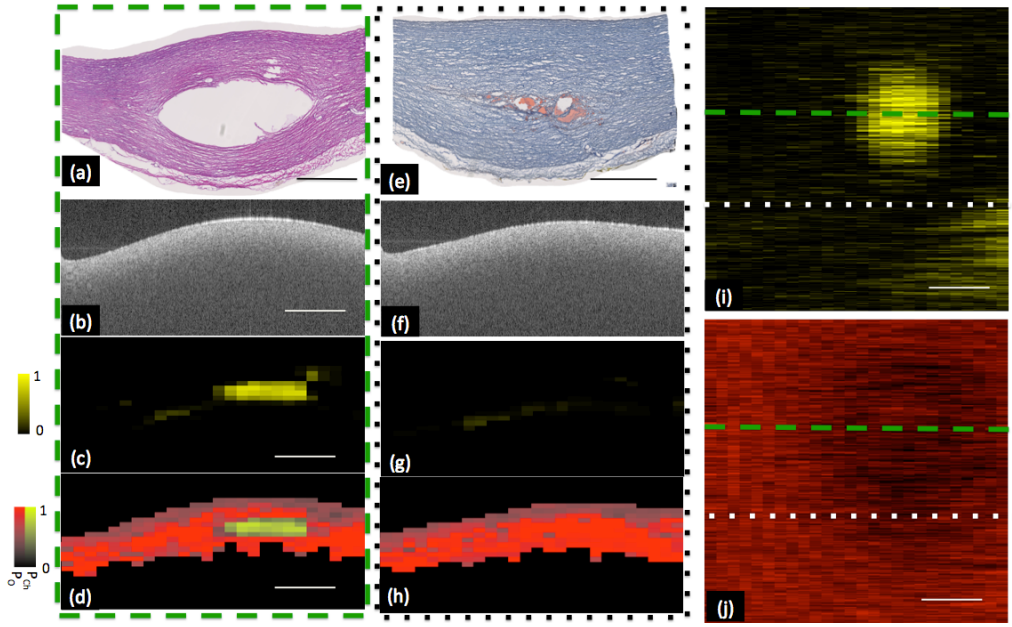

Fig. 8. Representative classification of lipid plaque phantom. Two sites within volumetric data set are shown in (a-d) and (e-h). (a,e) Histology taken through two cross sections within phantom plaque, showing void created by injection of fat emulsion. Corresponding H&E and oil-red-o stains respectively showing void created by the injection of a fat emulsion within center of plaque. (b, f) OFDI image of phantom lipid plaque corresponding to histology shown in panels a and e respectively. OFDI image shown in panel b is taken through the center of the artificial plaque whereas panel f is taken from the edge of the plaque. (c,g) Probability of cholesterol image derived from the output of the classification algorithm. A high probability of cholesterol is measured from the OFDI image taken through the center of the plaque. A low probability of cholesterol is measured through the edge of the plaque. (d, h) Classification and probability image utilizing a HSV convention where hue encodes class (red-other, yellow-cholesterol) and saturation and value encode probability. (i) Depth resolved integration of cholesterol probability. (j) Depth resolved integration of collagen probability. Within chemograms, lipid plaque can be seen as a circular region with increased cholesterol (i) and decreased collagen probability (j). Low probability of lipid was coded as black and high probability of lipid was coded as bright yellow. Low probability of collagen was coded as black and high probability of collagen was coded as bright red. Scale bar = 1mm.

The phantom plaques made by injecting fat emulsions had a cap thickness of 0.42mm ± –0.15mm (mean ± standard deviation) as measured by histology through the center of the plaque and lipid thickness 1.19mm ± –0.35mm (mean ± standard deviation) within the phantom plaque was measured as the void within the H&E frozen section analysis. Figure 9 shows regression analysis of fractions of pixels within the volume classified as collagen or cholesterol versus lipid thickness and cap thickness. Panel 9-A shows lipid thickness versus proportion of pixels classified as cholesterol. Regression analysis shows increased pixels classified as cholesterol with increasing lipid thickness. The relationship was significant, with p-value of 0.0158. In addition, normal areas with no lipid, had nearly zero pixels classified as cholesterol. Likewise, as the "cap" thickness increased, the proportion of pixels classified as cholesterol decreased, $p = 0.0138$. As lipid thickness increased, proportion of pixels classified as collagen decreased, $p = 0.0339$. However, collagen classified and cap thickness did not have a significant relationship. As shown in Fig. 9, proportion of pixels classified as cholesterol were significantly related to lipid thickness and cap thickness measured from histology slides, where cap was defined as the amount of tunica media overlying the lipid injection.

#189749 - $15.00 USD Received 2 May 2013; revised 14 Jun 2013; accepted 15 Jun 2013; published 5 Jul 2013

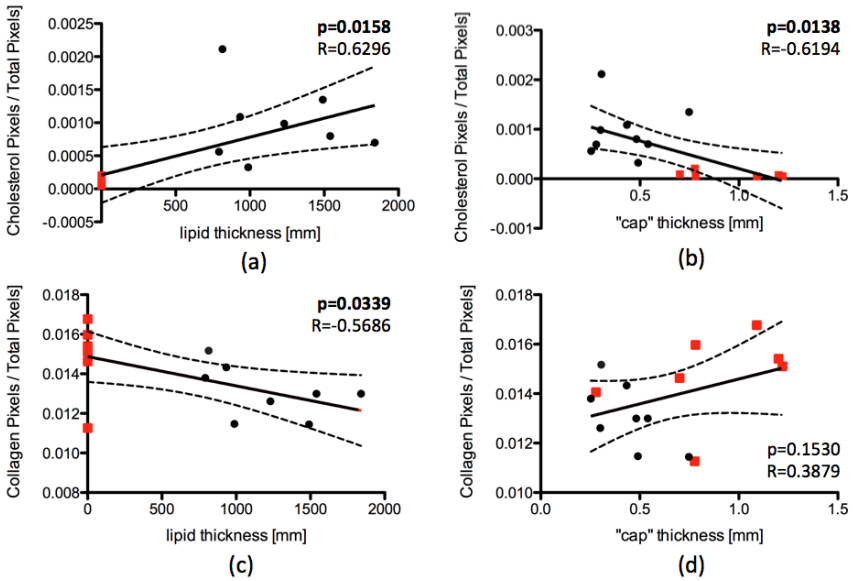

Fig. 9. Comparison of histology to classification of OFDI images by depth resolved spectral analysis. Lipid and cap thickness measured from histology slides versus fraction of pixels classified as cholesterol or collagen. Each point on the graph represents a separate sample. (a) Comparison of fraction of pixels classified as cholesterol to total pixels within volume versus lipid thickness measured from frozen histology slides at center of lipid plaque. Importantly, for three dimensional image sets of normal areas, nearly 0% of pixels were classified as cholesterol. (b) Comparison of fraction of pixels classified as cholesterol to total pixels with thickness of cap measured from frozen sections. We observed a significant negative trend, as cap thickness increases, the fraction of pixels classified as cholesterol decreases. We also observed a significant increase in pixels classified as cholesterol with increasing lipid thinness. (c) Comparison of the fraction of pixels classified as collagen versus lipid thickness has a significant negative trend, also observed within chemogram shown in 8i.(d) Comparison o fraction of pixels classified as collagen versus measured cap thickness did not have a significant correlation. Normal areas: red – squares, lipid plaques: black circles.

4. Discussion and conclusion

In this paper we have shown that a combined spectral and attenuation model, derived from the OCT data, can be used to accurately predict the presence of chemicals and molecules, including lipid, collagen, and calcium, in the OCT signal. Attenuation and backscattering analysis of axial scans using the single scattering model have been previously used to quantify the difference between fibro-calcific, fibrous, and lipid rich plaques. We have found that the combined model has significantly better accuracy than either spectral attenuation or magnitude of attenuation alone.

The model was validated both for chemical mixtures in a cuvette and a plaque phantom model based on injecting fat emulsions in the artery wall. To explore the roles contributing to spectral differences, phantoms of known with known chemical compositions and artificial lipid phantoms were imaged with an OFDI system. Cuvette based phantoms allowed us to evaluate the contributions for each component. Water has a linear increasing absorbance within our bandwidth, which is recapitulated using SOCT. Phantoms of just collagen and water have a relatively flat attenuation spectral slope. Our analytical phantom included the largest components within atherosclerotic plaques [25]. The phantom can be further expanded to include compositions with elastin, calcium carbonate, and cholesterol esters [25,34]. The analytical phantom model produced attenuation coefficients in the range of coronary arteries, but not as high as atherosclerotic plaques [14]. This may be due to the lower percentage of collagen used within our phantoms.

#189749 - $15.00 USD Received 2 May 2013; revised 14 Jun 2013; accepted 15 Jun 2013; published 5 Jul 2013

Using the analytical phantom model we demonstrated that the addition of spectral shape adds information to standard attenuation coefficient analysis. When combined the classification accuracy increased. However, our model was not able to reliably measure concentration of cholesterol or calcium and we therefore simplified the algorithm to assess the presence of each component.

To ensure that we were detecting spectral differences due to the presence of cholesterol and not just the reduce percentage of water, we imaged phantom compositions with mixtures of calcium. As shown in the confusion matrices in Fig. 5, the models have a low percentage of misclassification between cholesterol and calcium based phantoms. As shown in Jaross et al [25], the range of total cholesterol within a plaque was measured to be two to twenty-three percent, the range of water fifty four to seventy five percent, and collagen three to twenty one percent. Therefore our analytical model closely represents plaque composition.

Atherosclerotic plaques are heterogeneous, with components ranging from fibrin, red blood cells, smooth muscle cells [35], calcium, elastin [34], and infiltrates of macrophages [4]. In addition, these components are heterogeneous spatially and in composition. These features were not present within our lipid plaque phantom. Previous studies using image analysis has been conducted to detect the presence of macrophages [4] and calcium [36] and polarization sensitive OCT to discriminate collagen [37]. Therefore, our plaque addresses an important limitation within OCT imaging to reduce the ambiguity in detecting lipid within plaques.

Our classification model built upon previous studies that have shown that the attenuation coefficient is different between fibrous, lipid-rich, and calcific plaques [10–14]. Using time-frequency analysis to obtain depth resolved attenuation spectra. We added spectral shape as an additional parameter to improve classification of lipid. The STFT has a time-frequency trade-off. As applied to OCT images, that means there is a trade-off between spectral resolution and axial resolution. We choose to have increased spectral resolution at the expense of axial resolution. This is shown in the depth resolved probability maps in Figs. 7 and 8. Adjacent axial lines were averaged to increase the SNR of the spectrograms. Once the algorithm is translated to classification of human plaques with spatial heterogeneity and motion, averaging as many lines will not be feasible without blurring features.

Our tissue phantoms provided a simple way to create lipid plaques to test our algorithms. This allowed for analysis as to the limits of spectral analysis to measure the depth of a lipid pool and thickness of a fibrous cap. We conducted additional experiments with phantom plaques created with melted butter and vegetable oil (data not shown). Plaques created with the mayonnaise as the injectable fat emulsion was chosen because the scattering properties of mayonnaise aided in creating the qualitative appearance of a lipid plaque, which appears as diffuse borders within OCT images. In addition, compositions described in Table 1 were not viscous and could not be injected. The plaque model provided a test bed to analyze the algorithm in the setting of a known plaque composition. However, our plaque was created to feature only the lipid component of plaques. Within our model we were not able to create phantom plaques with cap thicknesses less than 100μm. The average plaque cap thickness created was 0.42mm ± −0.15mm (mean ± standard deviation). This limited our ability to further assess our algorithm with a thin-cap plaque model. In addition, due to the limited penetration depth of OFDI in the lipid phantom, the algorithm cannot quantify the volume of lipid. By analyzing the results from our phantom plaques, we were able to identify the limits to where the algorithm could accurately identify the presence of lipid/cholesterol. The SNR to which the algorithm failed was 24.98dB ± 7.7dB (mean ± STD).

Within the plaque phantom model we were able to assess detection of lipid below varying depths of medial tissue. Using a model based solely on the spectral fitting coefficients, we showed a significant increase in pixels classified as cholesterol with increasing lipid thickness as measured by frozen section histology analysis. Importantly, we showed that within aorta without the injection there were nearly no pixels classified as cholesterol (Fig. 9). Frozen

#189749 - $15.00 USD Received 2 May 2013; revised 14 Jun 2013; accepted 15 Jun 2013; published 5 Jul 2013

section analysis with H&E and ORO were able to show the dimensions of the plaque created, and within ORO stain the presence of lipid.

We developed a discriminant analysis model where we assumed that the samples imaged had a composition consisting of cholesterol, collagen, trioleate, and water. The model uses the spectral attenuation (scattering and absorption) of the samples to determine the probability that the sample is one of the compositions in Table 1. The lipid absorption is $0.02mm^{-1}$ and water $0.1mm^{-1}$ at our center wavelength of 1310 nm [38]. However, the water absorption increases to $0.3mm^{-1}$ at 1350nm [38], resulting in 30% absorption over 1mm. Therefore for water we will see a spectral dependent increase in water as shown in Fig. 4c. The spectral lipid absorption is $0.03mm^{-1}$ at 1250nm [38]. Taken together with the fact that scattering also decreases with increasing wavelength, within lipid/cholesterol we have a decreasing attenuation with increasing wavelength (Fig. 4b). It may be possible to further increase the accuracy of the technique if we increase the bandwidth of the light source. Within this study, we have shown that we can identify the presence of cholesterol. However, another metric for assessing vulnerability is to determine the proportion of types of cholesterol within a plaque. Cholesterol and cholesterol oleate have an absorption peak and slightly different spectral shapes around 1200 and 1700nm (Fig. 1). The utilization of a light source with a spectrum that overlaps the 1210 nm lipid absorption peak could enable easier identification of lipid and possibly even differentiation of types of cholesterols esters. A broader bandwidth light source that incorporates the 1200nm peak (Fig. 1a) will further improve extraction and possibly allow separation of scattering and absorption from the measured attenuation spectra [39,40]. This will enable easier identification of lipid absorption and enable differentiation of types of cholesterols esters.

The wavelength range of our existing OFDI source does not capture the peak of cholesterol absorption at 1200nm, we are sensitive to the tail portion. Within our current light source bandwidth, the absorbance for cholesterol decreases, whereas, water, which is a large component of fibrous tissue, has increased absorption at the end of our bandwidth. Although our bandwidth is not optimal for spectral analysis of cholesterol/lipid, the strength of this work is that we are operating at the wavelength range of current clinical intravascular imaging systems.

Scattering has two wavelength dependent features. First, scattering decreases nearly linearly with increasing wavelength. Secondly, scattering produces wavelength dependent modulations that corresponds to the scatter size and scatter density [41]. Within our analysis, we suppressed the second effect with preprocessing using the Salvosky Galoy polynomial filter. In the future, the modulation frequency can be used to identify additional features of plaque vulnerability such as macrophages.

Further validation of this method will make it possible to obtain chemical/molecular information from existing intracoronary OCT systems. An algorithm for automated classification of cholesterol plaques will enable easier and more accurate interpretation of intravascular OCT data sets by identifying depth resolved location of lipid. Our next step to accomplish this goal is to conduct a histological validation study of *ex vivo* atherosclerotic plaques in comparison with our classification model combining attenuation coefficient and spectral shape.

We demonstrated that the addition of spectral information, via spectroscopic OCT, can improve the accuracy of detecting cholesterol. This has important implications for depth localization of lipid and necrotic cores within coronary plaques. Importantly, with one system we incorporated both morphological and spectral analysis. The addition of spectral shape provided complementary information. By using models combining spectral shape with attenuation coefficient, we can reduce ambiguity when analyzing intravascular images. This may have important applications in a variety of applications where there is endogenous absorption contrast within the light source bandwidth.

#189749 - $15.00 USD Received 2 May 2013; revised 14 Jun 2013; accepted 15 Jun 2013; published 5 Jul 2013

Disclosure statement

Massachusetts General Hospital has a licensing arrangement with Terumo Corporation related to cardiovascular OFDI. Dr. Tearney has the rights to receive royalties resulting from this licensing arrangement. Dr. Tearney additionally receives royalties from St. Jude/Lightlab/MIT licensing arrangement related to OCT technology. Dr. Tearney receives sponsored research from Canon Inc. and consults for Samsung.

Acknowledgments

The authors would like to thank Apostolos Doukas, Bill Farinelli, and Melissa Haskell for their technical help. The project was supported in part by the National Institutes of Health (R01HL093717, NIH Diversity Supplement Postdoctoral Fellowship, Loan Repayment Award). The content is solely the responsibility of the authors and does not necessarily represent the official views of the National Heart Lung and Blood Institute or the National Institutes of Health.

#189749 - $15.00 USD Received 2 May 2013; revised 14 Jun 2013; accepted 15 Jun 2013; published 5 Jul 2013